



First-principles identification of topological crystalline insulators with C_2 rotation anomalyZhipeng Cao , Feng Tang, Di Wang, and Xiangang Wan *National Laboratory of Solid State Microstructures and School of Physics, Nanjing University, Nanjing 210093, China and Collaborative Innovation Center of Advanced Microstructures, Nanjing University, Nanjing 210093, China*

(Received 9 November 2020; accepted 29 March 2021; published 8 April 2021)

Recently, the concept of a rotation anomaly in the surface of C_n rotation ($n = 2, 4, 6$) protected topological crystalline insulators (TCIs) was proposed. However, verified material realizations of the rotation anomaly are still rare. Furthermore, owing to fruitful crystallographic symmetries, in addition to the rotation protected surface states, other kinds of topological boundary states could also emerge on suitable surfaces or hinges in one material, which is promising for manipulation in device applications. In this work, we identify a C_2 rotation anomaly in 24 TCIs and furthermore ascertain the positions of coexisting topological boundary states by first-principles calculations. Of these TCIs, using BiSe in space group 164 to illustrate, we demonstrate the mirror and C_2 rotation protected surface states in specific surfaces as well as the C_2 protected hinge states between two side surfaces. The predicated TCI materials with the C_2 rotation anomaly have diverse structures and chemical compositions and thus provide a good reference for future experimental studies.

DOI: [10.1103/PhysRevB.103.155113](https://doi.org/10.1103/PhysRevB.103.155113)**I. INTRODUCTION**

The study of topological materials has been a hot topic in condensed-matter physics and material science over the past around 15 years due to their novel electronic properties. The \mathbb{Z}_2 topological insulators (TIs) protected by time reversal symmetry (TRS) were proposed and realized in the early stage [1–3]. Other than internal symmetries like TRS, there exist fruitful crystallographic symmetries which can protect various topological crystalline insulator (TCI) phases [4,5], such as mirror Chern insulators [6], hourglass insulators protected by glide symmetries [7], and high-order TIs [8–12]. The introduction of crystallographic symmetries greatly enriched the topological phases of insulating electronic states.

Among these TCIs, the rotation protected TCIs have attracted broad research interest recently [13–19]. In these rotation protected TCIs, n massless Dirac fermions could emerge on the surface perpendicular to the n -fold rotation axis ($n = 2, 4, 6$) [13]. Throughout this work, we assume that time reversal symmetry T exists; namely, the investigated materials are all nonmagnetic, so that the C_n ($n = 2, 4, 6$) protected topology is C_n and T protected in essence, while we still use the terminology of C_n protection without ambiguity. These novel Dirac fermions cannot be realized in C_n -symmetric normal two-dimensional systems, thus dubbed a rotation anomaly [13]. These surface states with a rotation anomaly can be understood as the C_n ($n = 2, 4, 6$) generated n C_n and T protected Dirac states. Unlike mirror/glide symmetry protected surface states whose Dirac cones are pinned at high-symmetry lines, the Dirac cones of surface states corresponding to the rotation anomaly could be located at generic points in the surface Brillouin zone (BZ) possessing a higher tunability. Furthermore, n one-dimensional (1D) helical hinge states [13] could emerge along the hinges of a C_n -symmetric prism con-

figuration for C_n rotation protected TCIs. Up to now, several materials have been reported to host a rotation anomaly by first-principles calculations. For example, α -Bi₄Br₄ [14,19], Ba₃Cd₂As₄ [16], the transition metal dipnictide TaP₂ [17], and Bi [18] can have a C_2 rotation anomaly, while the Ca₂As family of materials can host a C_2 rotation anomaly when breaking mirror symmetry [15]. The rotation anomaly, coexisting with other exotic orders in solids, may open a new door to devices with low-energy consumption. Recently, the rotation anomaly in α -Bi₄Br₄ triggered the experimental study of the pressure induced superconductivity [20]. Remarkably, compared with other topological phases, the research on the rotation anomaly is relatively new both theoretically and experimentally, and the number of material realizations is still low. Hence, predicting more such materials is of important significance in regard to both fundamental research and device applications.

In order to discover rotation protected TCIs, one need to calculate the rotation topological invariant [13] in the conventional scheme. However, the conventional strategy is not very efficient for predictions by first-principles calculations since the calculations for the overlaps of wave functions usually cost much computer time. As a matter of fact, in realistic rotation protected TCIs, other crystallographic symmetries often exist in addition to the rotation symmetry. Utilization of these additional symmetries could accelerate the predictions of TCIs simply based on calculations of symmetry properties at high-symmetry momenta as exemplified by the method of symmetry indicators (SIs) [21] or topological quantum chemistry [22], with thousands of topological materials predicted [23–25]. In this work, we focus on C_2 rotation protected TCIs. The C_2 rotation anomaly is expected to be more common than those of C_4 and C_6 since C_4 and C_6 symmetries also imply C_2 symmetry. Our calculations are based on the database

TABLE I. All TCI materials with the C_2 rotation anomaly identified in this work. For them, the Fu-Kane-like formula for $(z_{2,1}, z_{2,2}, z_{2,3}, z_4)$ [27,28] in the $\mathbb{Z}_2 \times \mathbb{Z}_2 \times \mathbb{Z}_2 \times \mathbb{Z}_4$ SI key group (SG 2) is calculated by first-principles calculations. Together with the first-principles calculated MCN we can obtain the nonvanishing C_2 topological invariant, as shown in the fourth column through the mappings from SIs to topological invariants, and the double-stroke font represents the convention-independent case [27]. Note that the MCN is given in parentheses following the material name.

SG	SI $(z_{2,1}, z_{2,2}, z_{2,3}, z_4)$	MCN mod 4 ^a	C_2 ^b	Materials
12	(0,1,0,0)	2	1	Bi ₂ TeI [29] (2)
	(0,1,0,2)	0	1	ZrCl [30] (0)
	(1,0,1,2)	0	1	Ba ₃ Cd ₂ Sb ₄ [31] (0), BiHf ₂ [32] (0), Sc ₅ Cl ₈ N [33] (0)
	(1,1,1,2)	0	1	NbAs ₂ [34] (0), NbP ₂ [35] (0), NbSb ₂ [36] (0), TaAs ₂ [34] (0), TaSb ₂ [37] (0), Mo ₂ As ₃ [38] (0), W ₂ As ₃ [38] (0), Ta ₂ Te ₃ [39] (0), Ti ₃ Se ₄ [40] (0), ReGe ₂ [41] (0)
164	(0,0,1,0)	2	1	BiSe [42] (−2), BaSi ₂ [43] (2), BiTe [44] (−2), Bi ₃ Te ₂ S [45] (−2), Pb ₂ Bi ₂ Te ₅ [46] (−2)
166	(1,1,1,2)	0	1	LaBr [47] (0), ZrBr [48] (0), ZrCl [30] (0), Nb ₂ S ₂ C [49] (0)

^aFor SGs 12, 164, and 166, there is only one independent mirror plane, i.e., $(1\bar{1}0)$, (100) , and $(10\bar{1})$, respectively. The MCN can be any integer. However, a cutoff p is set here, and $-p < \text{MCN} \leq p$ for mapping from SIs to topological invariants [27]. For all three SGs, the corresponding p is 2. Therefore, here we give the result of MCN modulo 4.

^bFor SG 12, the C_2 rotation is $C_2^{1\bar{1}0}$. For SGs 164 and 166, it is C_2^{100} .

by Tang *et al.* [25]. Before the identification of C_2 rotation anomaly, we first filter out TCI materials for which the C_2 rotation anomaly is impossible. To identify the C_2 rotation anomaly efficiently, we focus on the space groups (SGs) for which we need to calculate only one mirror Chern number (MCN) [26–28] for the TCIs, based on which all possible coexisting TCI phases can thus be ascertained, including mirror protected TCI phases, weak TI phases, and C_2 protected high-order TI phases. We focus on only those nearly ideal TCIs with relatively clean Fermi surfaces and with the same SI results predicted by both the generalized gradient approximation (GGA) and the modified Becke-Johnson calculations [25]. In total, we find 24 TCI materials with a C_2 rotation anomaly, as listed in Table I, which are expected to be further studied by experiments. These materials with a C_2 rotation anomaly and other interesting topological crystalline phases could provide a new route to control the topological states in a material [50–53]. Here we choose BiSe crystallizing in SG 164 in Table I as the example to demonstrate the details of our calculations, including those of SIs, MCNs, and topological surface and hinge states. The TCI phases in other materials are also discussed, but the details are left to the Supplemental Material (SM) [54].

The rest of this paper is organized as follows. The computational methods are described in Sec. II. Then in Sec. III we demonstrate the details of calculations for identifying the C_2 rotation anomaly in BiSe (SG 164). Section IV A deals with rotation protected surface states, while Secs. IV B and IV C deal with mirror protected surface states and C_2 protected hinge states, respectively, both based on symmetry-respected Wannier models. The remaining materials with a C_2 rotation anomaly are discussed in Sec. V. Finally, a brief summary and discussion follow in Sec. VI.

II. COMPUTATIONAL METHODS

Our first-principles electronic structure calculations based on the density functional theory (DFT) are implemented by using the Vienna Ab initio Simulation Package (VASP) code [55,56]. We choose the Perdew-Burke-Ernzerhof functional of GGA as the exchange-correlation potential [57], and the pro-

jector augmented wave method is used to treat core-valence electron interactions [58,59]. Spin-orbit coupling is taken into account in all calculations. We use 1.5 times the maximum cutoff energy recommended in pseudopotential files as the plane wave cutoff energy and do the convergence test for k point parameters of every structure. The experiment crystal structures are used. The Z2PACK code interfaced with VASP is employed for MCN calculations [60,61]. For surface and hinge state calculations, high-quality tight-binding models under atom-centered Wannier functions have been constructed with the WANNIER90 code [62]. The calculations of surface constant-energy contours are completed by using the iterative Green's function method in the WANNIERTOOLS package [63,64].

III. IDENTIFICATION OF THE C_2 ROTATION ANOMALY IN BiSe

In this section, we take BiSe (SG 164) in Table I as the typical example to show detailed analyses and calculations. It crystallizes in a trigonal lattice [42] whose primitive unit cell is schematically shown in Fig. 1(b), which contains six chemical formulas in total. In BiSe, the bismuth bilayers are sandwiched by two Bi₂Se₃ quintuple layers [42]. The layered structure of BiSe may benefit the cleavages in experimental studies of its boundary electronic states. The stacking direction is along \mathbf{c} , as shown in Fig. 1(b). With respect to point symmetry, the point group of SG 164 is D_{3d} with 12 symmetry operators in total, of which three generators can be chosen to be inversion P , twofold rotation C_2^{100} , and threefold rotation C_3^{001} [here the direction of the rotation axis is expressed based on the basis lattice vectors \mathbf{a} , \mathbf{b} , \mathbf{c} shown in Fig. 1(b)]. Note that the other two C_2 rotations can be found through $C_2^{010} = C_2^{100}C_3^{001}$ and $C_2^{110} = C_3^{001}C_2^{100}$. Hence, there are three C_2 nonvanishing rotation invariants, corresponding to three sets of C_2 -symmetric surfaces (which are related by C_3 rotation) hosting the rotation anomaly. Three mirror operations can be obtained by the products of P and the three C_2 rotations, e.g., $M^{100} = PC_2^{100}$. As shown later, those mirror symmetries could guarantee the existence of six Dirac surface states in the mirror-symmetric (001) plane.

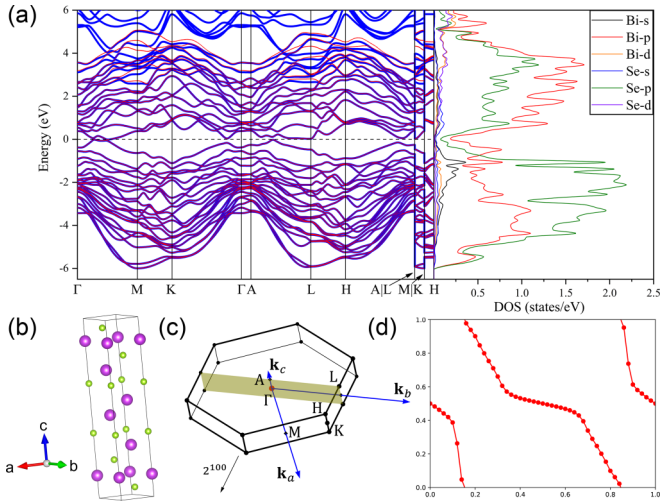


FIG. 1. (a) The electronic band structure of BiSe in SG 164, which shows a continuous and finite direct gap around the Fermi level (set to be 0 eV). The blue and red lines correspond to the band structures calculated by first-principles and the Wannier model, respectively. The orbital projected density of states for elements Bi and Se are also demonstrated. (b) The crystal structure of BiSe and \mathbf{a} , \mathbf{b} , \mathbf{c} define the lattice basis vectors of the hexagonal lattice. The purple and green balls denote Bi and Se atoms, respectively. (c) The BZ of SG 164 where \mathbf{k}_a , \mathbf{k}_b , \mathbf{k}_c are reciprocal lattice basis vectors with respect to \mathbf{a} , \mathbf{b} , \mathbf{c} . High-symmetry points Γ , M , A , H , L , K are shown. The C_2 rotation around the (100) direction is also shown, which is perpendicular to \mathbf{k}_b . The MCN calculation is performed in the shaded rectangle, namely, the \mathbf{k}_b - \mathbf{k}_c plane. (d) The evolution of the sum over occupied bands of HWCCs for a subspace with mirror eigenvalue $+i$ along \mathbf{k}_b , where the horizontal axis is in units of k_b , while the vertical axis is in units of 2π .

The first-principles electronic band structure of BiSe along high-symmetry points [Γ , M , K , A , L , H ; see Fig. 1(c)] is shown in Fig. 1(a). Although there is no full gap according to the density of states as shown in Fig. 1(a), we carefully check the eigenvalues of energy bands and find that there is a continuous finite direct gap within the whole BZ, so that the MCN can be well defined. In addition, the Fermi surfaces are relatively clean, so we expect the topological boundary states can be clearly demonstrated in some suitable energy-momentum window. On the basis of the orbital projected density of states shown in Fig. 1(a), around the Fermi level, we found that the $4p$ orbitals of Se dominate in the energy range from -6.5 to 0 eV, while the $6p$ orbitals of Bi dominate in the energy range from 0 to 4 eV. Since each Se atom contributes 4 valence electrons while each Bi contributes 3 valence electrons, there are, in total, 42 valence electrons in one primitive unit cell. Hence, the filling number is 42. We reproduce the same result for n_k^j [the number of occurrences of the j th irreducible representations (irreps) of the little group of high-symmetry points k] as Ref. [25] for the 42 valence bands, as shown below:

$$\begin{aligned} n &= (v, n_\Gamma^1 = 3, n_\Gamma^2 = 3, n_\Gamma^3 = 8, n_\Gamma^4 = 3, n_\Gamma^5 = 3, n_\Gamma^6 = 7, \\ n_M^1 &= 10, n_M^2 = 10, n_M^3 = 11, n_M^4 = 11, \\ n_A^1 &= 3, n_A^2 = 3, n_A^3 = 7, n_A^4 = 3, n_A^5 = 3, n_A^6 = 8, \end{aligned}$$

$$\begin{aligned} n_L^1 &= 11, n_L^2 = 11, n_L^3 = 10, n_L^4 = 10, \\ n_K^1 &= 7, n_K^2 = 7, n_K^3 = 14, \\ n_H^1 &= 7, n_H^2 = 7, n_H^3 = 14. \end{aligned} \quad (1)$$

Here $v = 42$ is the filling number, and Γ , M , A , L , K , H are high-symmetry points [65]. For Γ , M , A , L , K , H , there are 6, 4, 6, 4, 3, and 3 irreps, respectively [65]. The order of irreps follows that in Ref. [65]. n in Eq. (1) can be expanded on the nine atomic basis vectors a_i , $i = 1, 2, \dots, 9$ (where a_8 has a common factor of 2, while a_9 has a common factor of 4, corresponding to \mathbb{Z}_2 and \mathbb{Z}_4 , respectively, and the rest have no common factor) [14,21]. It is found that $n = 3a_1 - a_4 - a_6 + \frac{1}{2}a_8 + \frac{1}{2}a_9$, so that BiSe is a TCI [14] whose SI takes (1,2) in the $\mathbb{Z}_2 \times \mathbb{Z}_4$ SI group for SG 164.

As indicated by the nonvanishing SI, band inversion should occur somewhere in the BZ. We thus calculate the parity at eight time reversal invariant momenta (TRIM), which include one Γ , one A , three M 's, and three L 's. The numbers of occupied Kramers pairs with negative parity at TRIM are 10, 11, 11, and 10 for Γ , A , M , and L , respectively. Based on the results of parities, we can calculate $z_{2,1}$, $z_{2,2}$, $z_{2,3}$, z_4 [27,28] as defined for the SI group $\mathbb{Z}_2 \times \mathbb{Z}_2 \times \mathbb{Z}_2 \times \mathbb{Z}_4$ of SG $2 \subset$ SG 164 (SG 2 is called the key SI group) by $z_{2,j} = \sum_{k \in \text{TRIM}, k_j = \pi} n_k^- \text{mod} 2$ and $z_4 = \sum_{k, k \in \text{TRIM}} \frac{n_k^- - n_k^+}{2} \text{mod} 4$, where n_k^{\pm} represent the number of occupied Kramers pairs with even and odd parity, respectively. We found that $(z_{2,1}, z_{2,2}, z_{2,3}, z_4) = (0, 0, 1, 0)$, which shows that BiSe is a weak TI due to the nonvanishing weak topological index $z_{2,3}$ [27,28]. Furthermore, the result that $z_{2,3} = 1$ means that an even number of Dirac cones in the (100) and (010) surfaces exists [66]. The inversion topological invariant z_4 [27,28] is zero, indicating that no inversion protected hinge states exist in BiSe. We then investigate the possible TCI phases protected by rotation and mirror symmetries.

For that we calculate the hybrid Wannier charge centers (HWCCs) [67] along the shaded rectangle shown in Fig. 1(c) and show the sum of HWCCs for the subspace with the mirror eigenvalue being $+i$ in Fig. 1(d). We conclude that the MCN is -2 from Fig. 1(d). According to the mapping table between SIs and topological invariants listed in [27], in the case of SG 164, there are two possible sets of topological invariants when the SI $(z_{2,1}, z_{2,2}, z_{2,3}, z_4) = (0, 0, 1, 0)$. For one set, the MCN is equal to zero, and the rotation invariant of C_2^{100} is also equal to zero. For the other one, these two invariants are equal to 2 and 1, respectively. Because the MCN we calculate is $-2 = 2 \pmod{4}$, the C_2^{100} rotation invariant should be 1; thus, BiSe could host a C_2 rotation anomaly in C_2 symmetry respected surfaces and C_2 protected hinge states along the C_2 -symmetric prism. In the following, we first obtain a reasonable Wannier model which not only reproduces the first-principles calculated band structure very well but also has exactly the same n and MCN and then apply this model to calculate the topological protected boundary states implied by the nontrivial bulk topology.

IV. TOPOLOGICAL BOUNDARY STATES IN BiSe

As pointed out before, the dominant orbitals around the energy range of -6.5 to 4 eV of the band structure come

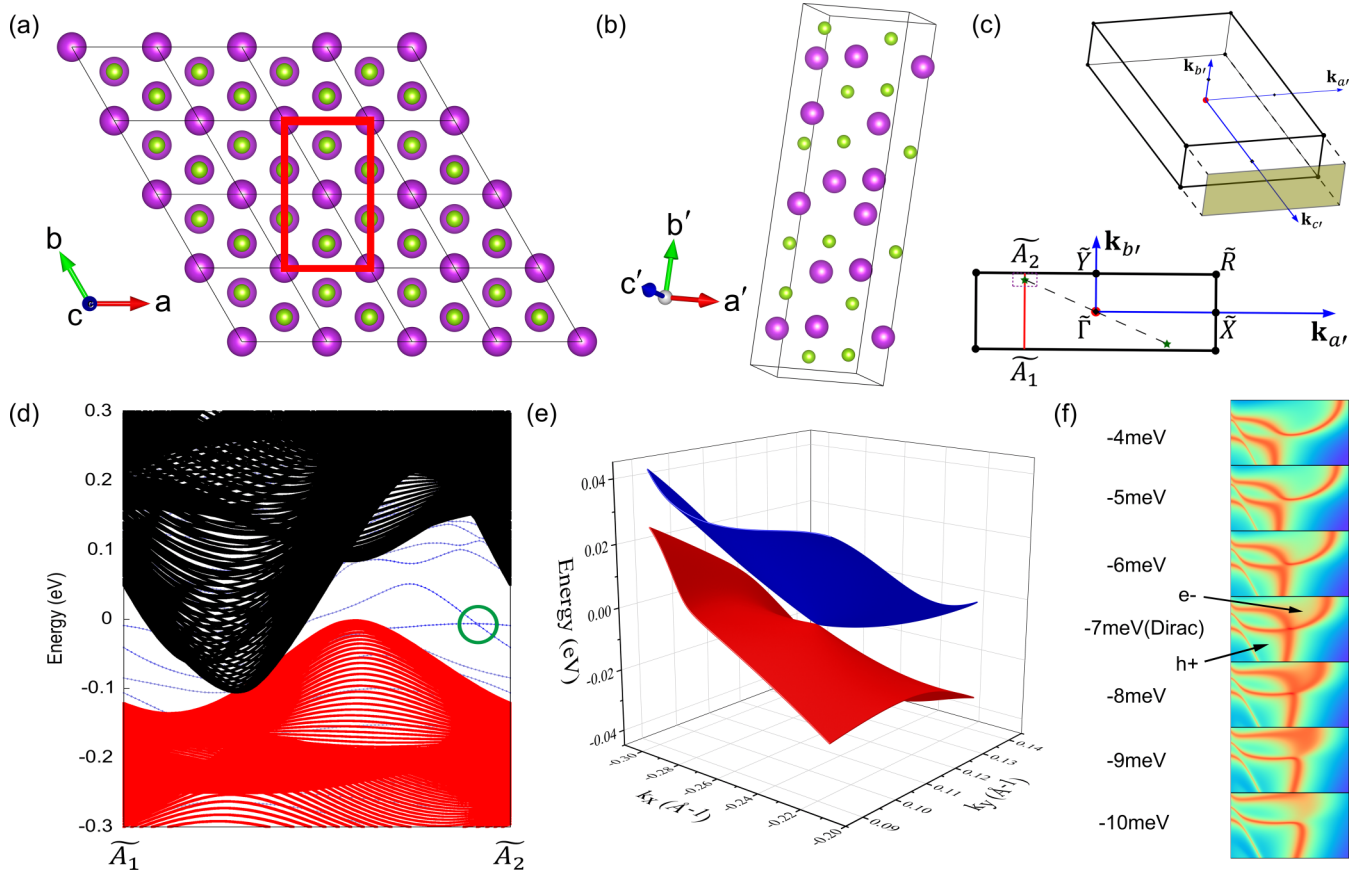


FIG. 2. (a) To construct a slab with C_2^{100} rotation symmetry, we choose different lattice basis vectors as shown in (b): $\mathbf{a}' = \mathbf{a} + 2\mathbf{b}$, $\mathbf{b}' = \mathbf{c}$, $\mathbf{c}' = \mathbf{a}$, which are perpendicular to each other so that \mathbf{c}' is perpendicular to \mathbf{a}' and \mathbf{b}' . Here we show the top view of the lattice, and the red frame indicates the new unit cell in the \mathbf{a} - \mathbf{b} plane. (b) New lattice basis vectors \mathbf{a}' , \mathbf{b}' , \mathbf{c}' . (c) The orthorhombic reciprocal BZ with respect to the new lattice basis vectors is shown in the top panel: The reciprocal lattice basis vectors \mathbf{k}'_a , \mathbf{k}'_b , \mathbf{k}'_c are also shown, as well as the surface BZ for the (100) surface. In the bottom panel, we show the positions of two Dirac cones in the surface BZ for the C_2 rotation anomaly by two green stars, which are related by time reversal or inversion. (d) The electronic band structure for the slab described in (a) based on the Wannier model for BiSe along the path shown in (c), namely, $\tilde{A}_1 - \tilde{A}_2$, which just crosses one of the two Dirac cones, as indicated by the green circle here. The blue curves correspond to surface states and are twofold degenerate due to the Kramer's theorem. The surface states connect the projected bands of valence bands and conduction bands (red and black regions, respectively). (e) The energy band structures of the zone containing a Dirac cone in the (100) surface BZ. (f) To verify the type-II character of the Dirac cone for the C_2 rotation anomaly, we plot the energy contour for different energies. e^- and h^+ denote an electron pocket and hole pocket, respectively.

from p orbitals from Bi and Se. We use these orbitals as the initial guess of Wannier functions. The band structure of the obtained Wannier model is shown by red curves in Fig. 1(a), fitting the DFT bands (blue curves) very well. It is worth mentioning that our Wannier model also respects the spatial symmetries well. This is based on checking the transformation of Wannier basis functions under operations in SG 164. The Bloch eigenstates for the 42 occupied bands of the Wannier model at high-symmetry points Γ, M, A, L, K, H are used to calculate the representations of their little groups, and thus the numbers (n_k^j) are found, exactly the same as Eq. (1). Hence, the Wannier model has the same SI in $\mathbb{Z}_2 \times \mathbb{Z}_4$ for SG 164, and $(z_{2,1}, z_{2,2}, z_{2,3}, z_4)$ for the Wannier model is also exactly the same as those found by first-principles calculations. In addition, the MCN for the shaded rectangle as in Fig. 1(c) is -2 for the Wannier model, the same as the first-principles one. Hence, we expect that the Wannier model could demonstrate topological surface/hinge states of BiSe reasonably.

A. C_2 rotation anomaly

Though the C_2 invariant in BiSe (SG 164) can be trivialized by choosing a different origin [27], the rotation anomaly can still be observed in the surface which is symmetric under C_2 whose fixed point coincides with the origin we adopted to calculate the SI. In order to demonstrate the C_2 rotation anomaly, we should construct a slab which preserves C_2 symmetry. Here we choose the C_2 symmetry around the (100) direction, while the other two C_2 rotations can be related by C_3 around \mathbf{c} . As shown in Figs. 2(a) and 2(b), we choose a new unit cell whose basis vectors are expressed as $\mathbf{a}' = \mathbf{a} + 2\mathbf{b}$, $\mathbf{b}' = \mathbf{c}$, and $\mathbf{c}' = \mathbf{a}$. It is easy to find that \mathbf{c}' is perpendicular to \mathbf{a}' and \mathbf{b}' ; thus, it is convenient for the C_2 symmetry around \mathbf{a} (\mathbf{c}') to be fulfilled. As shown in the top view in Fig. 2(a), the red frame representing the new unit cell in the ab plane possesses C_2 symmetry. We take the open boundary condition along \mathbf{c}' , and the slab is infinite in the other two directions. Based on the Wannier model for BiSe, we thus obtain the electronic

band structure of the slab through direct diagonalization for the surface BZ, namely, the shaded rectangle in Fig. 2(c). Two surface Dirac cones for the rotation anomaly are found based on their real-space distribution of the Bloch states, and they are located at $\pm(0.297\mathbf{k}'_a - 0.41\mathbf{k}'_b)$, where \mathbf{k}'_a and \mathbf{k}'_b are the reciprocal lattice basis vectors corresponding to \mathbf{a}' , \mathbf{b}' , \mathbf{c}' . They are indicated by two green stars in Fig. 2(c). In order to verify the surface Dirac cone, we choose a loop enclosing it in the (100) surface BZ and calculate the Berry phase of wave functions of surface states. The corresponding details are demonstrated in the SM [54], and a result close to π is acquired, which verifies the existence of the C_2 rotation anomaly Dirac cone. To display the band plot of the surface Dirac states, we choose the path to be $\tilde{A}_1 - \tilde{A}_2$ as in Fig. 2(c), which just crosses one of the two Dirac points. The calculated bands of the slab for that path are shown in Fig. 2(d), where the red and black regions represent the bulk band projections of valence and conduction bands, while the blue curves, connecting the valence and conduction bulk bands, are bands of surface states. Note that the blue curves are twofold degenerate due to the Kramers degeneracy by PT symmetry because the slab we use also has an inversion center. The circle in Fig. 2(d) indicates the position of one Dirac point. Furthermore, a three-dimensional plot of energy bands of surface states around the C_2 protected Dirac point is shown in Fig. 2(e). It can be found that the Dirac point is tilted or of type-II character, which is verified by the energy contour plots in Fig. 2(f). The Dirac cones with respect to the C_2 rotation anomaly are located at generic positions in the surface BZ and can be tuned to move by C_2 and time reversal preserved perturbations. Next, we study the mirror ($M^{100} = PC_2^{100}$) protected surface states.

B. Mirror protected surface states

The surface we take above for the calculation of the C_2 rotation anomaly is actually not invariant under mirror operation; thus, the mirror protected surface states are expected to emerge in other surfaces. As a matter of fact, the (001) surface, whose BZ is shown in Fig. 3(a), can host such surface states. We choose a slab with finite length in the (001) direction but infinite length in the other two directions. The surface is actually invariant under M^{100} mirror symmetry as well as C_3^{001} symmetry. Hence, the surface is symmetric under all three mirror operations. The slab we use is also found to have inversion symmetry such that the electronic bands of the slab should be at least twofold degenerate due to Kramers theorem. In addition, to demonstrate the mirror protected surface Dirac states in the (001) surface, we need to plot only the band structure in the $\tilde{\Gamma}-\tilde{L}$ path shown in Fig. 3(a) since the other Dirac points can be obtained by C_3 or T . Note that the $\tilde{\Gamma}-\tilde{L}$ path is invariant under M^{100} . The band structure along that path is shown in Fig. 3(b), from which the surface states are found to traverse the gap between the valence and conduction bands (red and black, respectively). The blue curves cross each other, resulting in a Dirac cone, as denoted by the green circle. Due to time reversal symmetry or inversion symmetry, there is another Dirac point in the $-\mathbf{k}_b$ direction, consistent with the result of MCN ($= -2$). Considering C_3^{001} symmetry, there will be six Dirac cones in the (001) surface BZ.

C. C_2 protected hinge states

In addition to the topologically protected surface states by rotation and mirror, it is also predicted that two 1D helical hinge states along the hinge formed by two side surfaces parallel to the C_2 rotation axis will be found [13]. In order to catch such hinge states, we then construct a prism along the (100) direction, preserving C_2^{100} rotation symmetry. First, we choose a set of new lattice basis vectors defined as $\mathbf{a}'' = \mathbf{a} + 2\mathbf{b}$, $\mathbf{b}'' = 2\mathbf{a} + 4\mathbf{b} + \mathbf{c}$, and $\mathbf{c}'' = \mathbf{a}$. Apparently, \mathbf{c}'' is perpendicular to the other basis vectors, and it is thus convenient to impose C_2 symmetry around \mathbf{c}'' [the original (100) direction]. The prism is thus along \mathbf{c}'' , in which direction the length is infinite. In the other two directions, the boundary conditions are open. The top view of the prism is schematically shown in the xy plane in Fig. 3(c). Based on the Wannier model we constructed, which reproduces the first-principles results of BiSe very well, we calculate the electronic band structure of the C_2 -symmetric prism, shown in Fig. 3(d). Through the real-space distribution of the Bloch wave functions, we could identify the bulk and surface states corresponding to the red and black regions in Fig. 3(d), and the hinge states represented by blue curves are found. Since the prism we take is found to be inversion symmetric, the bands of the hinge states are twofold degenerate. The specific real-space distribution of the wave functions of hinge states is shown in Fig. 3(c). Considering the motion in the direction of \mathbf{c}'' , the hinge states thus constitute a helical pattern, as predicted by the nontrivial band topology.

V. OTHER C_2 PROTECTED TCIs

As displayed in Table I for all 24 TCIs with C_2 rotations, they have diverse topological properties other than the non-vanishing C_2 topological invariant. It should be noted that the C_2 invariant is convention independent in the case when the SG is 12, SI is (1,0,1,2), and MCN is zero [27]. This fact means that the C_2 rotation anomaly is physical for $\text{Ba}_3\text{Cd}_2\text{Sb}_4$, BiHf_2 , and $\text{Sc}_5\text{Cl}_8\text{N}$. The details of the calculations for all 24 TCIs are left to the SM [54]. It can be found that all these materials have nonvanishing weak topological indices from the calculated $z_{2,j}$, $j = 1, 2, 3$. Hence, there TCIs could host translation protected surface states in suitable surfaces. The inversion invariant z_4 can take only two values, 0 or 2; otherwise, the material will be a TI [27,28]. Interestingly, when $z_4 = 0$, the MCN is a nonvanishing even number from Table I. And when $z_4 = 2$, the MCN is vanishing. $z_4 = 2$ means that the TCI could host inversion protected hinge states [27,28] other than the C_2 protected ones. It is worth mentioning that when surface states that can be protected simultaneously by mirror and C_2 symmetries exist, we need to break both symmetries to gap the surface states. When the mirror symmetry is broken, the surface Dirac cones could then move to generic positions in the surface BZ. And when the C_2 symmetry is broken, the surface Dirac cones can still be protected by the mirror symmetry to lie in high-symmetry lines in the surface BZ, but with modifications in the low-energy Dirac physics (e.g., generating more anisotropy). Furthermore, the surface and hinge states may coexist in one material, possibly providing a novel way of manipulating the different types of

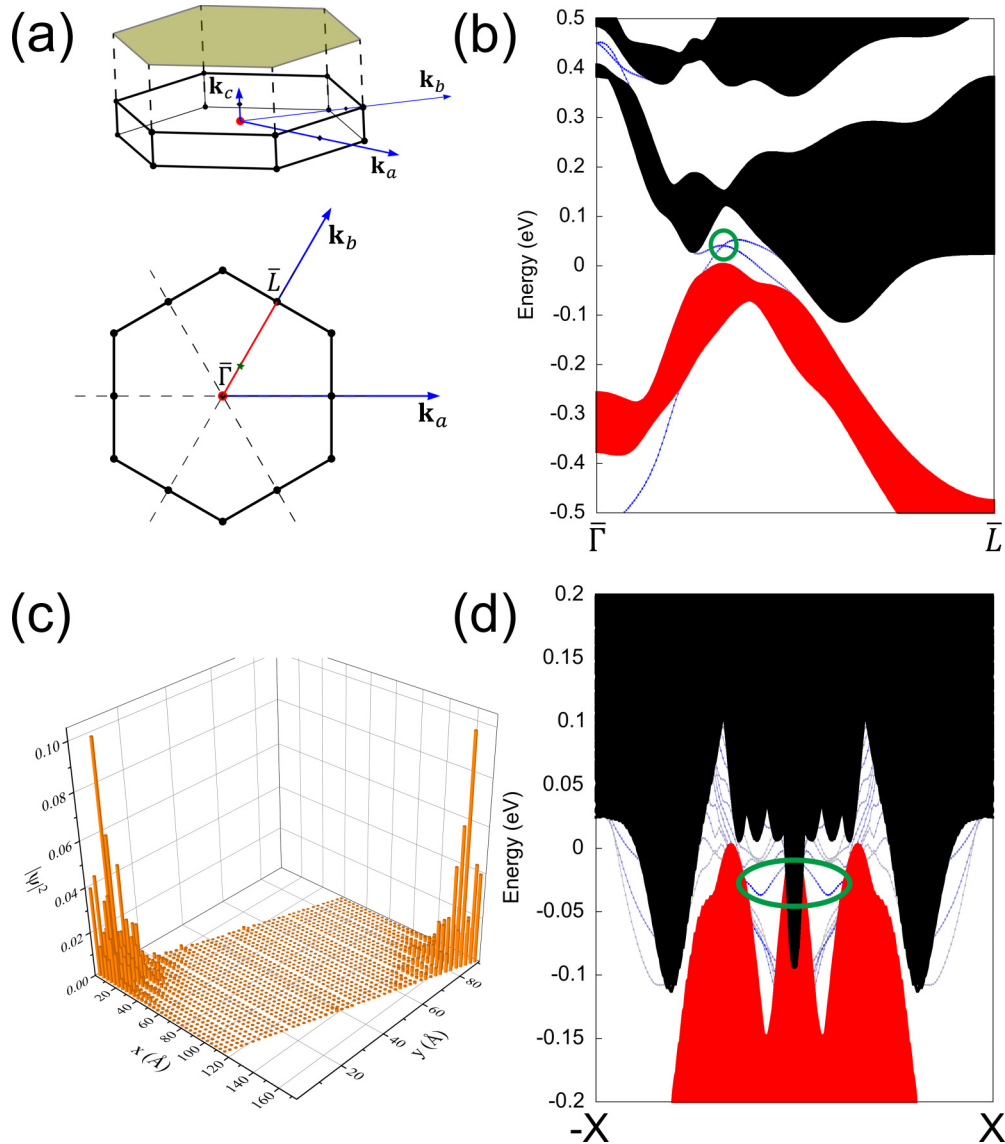


FIG. 3. (a) The surface BZ of the (001) surface is shown by the shaded hexagon in the top panel, while in the bottom panel, $\bar{\Gamma}-\bar{L}$, which is invariant under mirror operation M^{100} , shows a Dirac cone, as indicated by the green star. (b) The electronic band structure of the slab which preserves M^{100} mirror symmetry and has finite length in the (001) direction based on the Wannier model of BiSe and along $\bar{\Gamma}-\bar{L}$ in (a). The circle denotes the position of the Dirac cone for the surface states, for which two surface bands represented by blue curves cross each other and connect the projections of conduction (black) and valence (red) bands. Each band is twofold degenerate due to the coexistence of time reversal symmetry and inversion symmetry. (c) The real-space distribution of hinge state wave functions, where each site in the xy plane represents an atom from the top view of the prism to calculate the hinge states. (d) The electronic structure of the prism for C_2 protected hinge states based on the Wannier model of BiSe where $X = \frac{\pi}{c^*}$. Red and black denote the bands projected from the bulk and surfaces, while the blue curves denote the hinge states. The prism we take also has inversion symmetry other than C_2 symmetry, so that each band is twofold degenerate. The positions of hinge states in the green circle are schematically shown in (c) by two red circles.

topological boundary states, which may be useful for transport study or device application.

VI. CONCLUSIONS AND DISCUSSION

In summary, through first-principles calculations we checked suitable TCI materials from the database established by Tang *et al.* [25] and predicted 24 materials in total with a C_2 rotation anomaly in their C_2 -symmetric surfaces. Among these rotation anomaly materials, $\text{Ba}_3\text{Cd}_2\text{Sb}_4$, BiHf_2 , and $\text{Sc}_5\text{Cl}_8\text{N}$ have the physical C_2 protected nontrivial topology.

Other kinds of TCI phases, including weak TIs, mirror protected TCIs, and C_2 protected high-order TIs, which may coexist in one material were also explored. Our calculations are based on SIs combined with the MCN calculation, and then all other topological invariants can be found [27,28]. Our results suggest that all 24 materials here are also weak TIs. Furthermore, Bi_2TeI in SG 12 and all of the predicted materials in SG 164 have MCN equal to 2. We take BiSe in SG 164 as the illustrative example to show detailed analyses in the main text: With the same n as Ref. [25], we conclude that the material has the same SI in the SI group ($\mathbb{Z}_2 \times \mathbb{Z}_4$) [21].

Since the parent group is SG 2, we thus calculated $z_{2,1}, z_{2,2}, z_{2,3}, z_4 \in \mathbb{Z}_2 \times \mathbb{Z}_2 \times \mathbb{Z}_2 \times \mathbb{Z}_4$ (the SI group of SG 2) to further survey all TCI phases [27,28]. Then the rotation anomaly, mirror Chern insulator, weak TI, and high-order band TI phases in this material were identified from the MCN with respect to the (100) mirror plane. We thus constructed a Wannier model not only fitting the electronic band structure well but reproducing the same n and MCN. Based on the Wannier model, we observed two type-II Dirac cones located at generic points on the (100) surface due to the rotation anomaly, while six Dirac cones appeared on the (001) surface due to the finite MCN ($= -2$; C_3 -related Dirac cones are enumerated). Other than topological surface states, 1D helical hinge states could also appear. We expect that our results pro-

vide a good platform for further theoretical and experimental studies.

ACKNOWLEDGMENTS

We were supported by the National Key R&D Program of China (Grants No. 2017YFA0303203 and No. 2018YFA0305704), the National Natural Science Foundation of China (NSFC Grants No. 11834006, No. 12004170, No. 51721001, and No. 11790311), and the excellent program at Nanjing University. X.W. also acknowledges the support from the Tencent Foundation through the XPLOER PRIZE. F.T. was supported by the Fundamental Research Fund for the Central Universities (Grants No. 14380144 and No. 14380157).

-
- [1] M. Z. Hasan and C. L. Kane, Colloquium: Topological insulators, *Rev. Mod. Phys.* **82**, 3045 (2010).
- [2] X.-L. Qi and S.-C. Zhang, Topological insulators and superconductors, *Rev. Mod. Phys.* **83**, 1057 (2011).
- [3] A. Bansil, H. Lin, and T. Das, Colloquium: Topological band theory, *Rev. Mod. Phys.* **88**, 021004 (2016).
- [4] Y. Ando and L. Fu, Topological crystalline insulators and topological superconductors: From concepts to materials, *Annu. Rev. Condens. Matter Phys.* **6**, 361 (2015).
- [5] L. Fu, Topological Crystalline Insulators, *Phys. Rev. Lett.* **106**, 106802 (2011).
- [6] T. H. Hsieh, H. Lin, J. Liu, W. Duan, A. Bansil, and L. Fu, Topological crystalline insulators in the SnTe material class, *Nat. Commun.* **3**, 982 (2012).
- [7] Z. Wang, A. Alexandradinata, R. J. Cava, and B. A. Bernevig, Hourglass fermions, *Nature (London)* **532**, 189 (2016).
- [8] W. A. Benalcazar, B. A. Bernevig, and T. L. Hughes, Quantized electric multipole insulators, *Science* **357**, 61 (2017).
- [9] W. A. Benalcazar, B. A. Bernevig, and T. L. Hughes, Electric multipole moments, topological multipole moment pumping, and chiral hinge states in crystalline insulators, *Phys. Rev. B* **96**, 245115 (2017).
- [10] Z. Song, Z. Fang, and C. Fang, $(d-2)$ -Dimensional Edge States of Rotation Symmetry Protected Topological States, *Phys. Rev. Lett.* **119**, 246402 (2017).
- [11] J. Langbehn, Y. Peng, L. Trifunovic, F. von Oppen, and P. W. Brouwer, Reflection-Symmetric Second-Order Topological Insulators and Superconductors, *Phys. Rev. Lett.* **119**, 246401 (2017).
- [12] F. Schindler, A. M. Cook, M. G. Vergniory, Z. Wang, S. S. P. Parkin, B. A. Bernevig, and T. Neupert, Higher-order topological insulators, *Sci. Adv.* **4**, eaat0346 (2018).
- [13] C. Fang and L. Fu, New classes of topological crystalline insulators having surface rotation anomaly, *Sci. Adv.* **5**, eaat2374 (2019).
- [14] F. Tang, H. C. Po, A. Vishwanath, and X. Wan, Efficient topological materials discovery using symmetry indicators, *Nat. Phys.* **15**, 470 (2019).
- [15] X. Zhou, C.-H. Hsu, T.-R. Chang, H.-J. Tien, Q. Ma, P. Jarillo-Herrero, N. Gedik, A. Bansil, V. M. Pereira, S.-Y. Xu, H. Lin, and L. Fu, Topological crystalline insulator states in the Ca_2As family, *Phys. Rev. B* **98**, 241104(R) (2018).
- [16] T. Zhang, C. Yue, T. Zhang, S. Nie, Z. Wang, C. Fang, H. Weng, and Z. Fang, Topological crystalline insulators with C_2 rotation anomaly, *Phys. Rev. Res.* **1**, 012001(R) (2019).
- [17] B. Wang, B. Singh, B. Ghosh, W.-C. Chiu, M. M. Hosen, Q. Zhang, L. Ying, M. Neupane, A. Agarwal, H. Lin, and A. Bansil, Topological crystalline insulator state with type-II Dirac fermions in transition metal dipnictides, *Phys. Rev. B* **100**, 205118 (2019).
- [18] C.-H. Hsu, X. Zhou, T.-R. Chang, Q. Ma, N. Gedik, A. Bansil, S.-Y. Xu, H. Lin, and L. Fu, Topology on a new facet of bismuth, *Proc. Natl. Acad. Sci. USA* **116**, 13255 (2019).
- [19] C.-H. Hsu, X. Zhou, Q. Ma, N. Gedik, A. Bansil, V. M. Pereira, H. Lin, L. Fu, S.-Y. Xu, and T.-R. Chang, Purely rotational symmetry-protected topological crystalline insulator $\alpha\text{-Bi}_4\text{Br}_4$, *2D Mater.* **6**, 031004 (2019).
- [20] X. Li, D. Chen, M. Jin, D. Ma, Y. Ge, J. Sun, W. Guo, H. Sun, J. Han, W. Xiao, J. Duan, Q. Wang, C.-C. Liu, R. Zou, J. Cheng, C. Jin, J. Zhou, J. B. Goodenough, J. Zhu, and Y. Yao, Pressure-induced phase transitions and superconductivity in a quasi-1-dimensional topological crystalline insulator $\alpha\text{-Bi}_4\text{Br}_4$, *Proc. Natl. Acad. Sci. USA* **116**, 17696 (2019).
- [21] H. C. Po, A. Vishwanath, and H. Watanabe, Symmetry-based indicators of band topology in the 230 space groups, *Nat. Commun.* **8**, 50 (2017).
- [22] B. Bradlyn, L. Elcoro, J. Cano, M. G. Vergniory, Z. Wang, C. Felser, M. I. Aroyo, and B. A. Bernevig, Topological quantum chemistry, *Nature (London)* **547**, 298 (2017).
- [23] T. Zhang, Y. Jiang, Z. Song, H. Huang, Y. He, Z. Fang, H. Weng, and C. Fang, Catalogue of topological electronic materials, *Nature (London)* **566**, 475 (2019).
- [24] M. G. Vergniory, L. Elcoro, C. Felser, N. Regnault, B. A. Bernevig, and Z. Wang, A complete catalog of high-quality topological materials, *Nature (London)* **566**, 480 (2019).
- [25] F. Tang, H. C. Po, A. Vishwanath, and X. Wan, Comprehensive search for topological materials using symmetry indicators, *Nature (London)* **566**, 486 (2019).
- [26] J. C. Y. Teo, L. Fu, and C. L. Kane, Surface states and topological invariants in three-dimensional topological insulators: Application to $\text{Bi}_{1-x}\text{Sb}_x$, *Phys. Rev. B* **78**, 045426 (2008).
- [27] Z. Song, T. Zhang, Z. Fang, and C. Fang, Quantitative mappings between symmetry and topology in solids, *Nat. Commun.* **9**, 3530 (2018).
- [28] E. Khalaf, H. C. Po, A. Vishwanath, and H. Watanabe, Symmetry Indicators and Anomalous Surface States of Topological Crystalline Insulators, *Phys. Rev. X* **8**, 031070 (2018).

- [29] S. V. Savilov, V. N. Khrustalev, A. N. Kuznetsov, B. A. Popovkin, and M. Yu. Antipin, New subvalent bismuth telluroiodides incorporating Bi_2 layers: The crystal and electronic structure of Bi_2TeI , *Russ. Chem. Bull.* **54**, 87 (2005).
- [30] D. G. Adolphson and J. D. Corbett, Crystal structure of zirconium monochloride. A novel phase containing metal-metal bonded sheets, *Inorg. Chem.* **15**, 1820 (1976).
- [31] B. Saparov, S. Xia, and S. Bobev, Synthesis, structure, and bonding of the Zintl phase $\text{Ba}_3\text{Cd}_2\text{Sb}_4$, *Inorg. Chem.* **47**, 11237 (2008).
- [32] O. Levy, G. L. W. Hart, and S. Curtarolo, Hafnium binary alloys from experiments and first principles, *Acta Mater.* **58**, 2887 (2010).
- [33] S.-J. Hwu, D. S. Dudis, and J. D. Corbett, Synthesis, structure, and properties of the infinite-chain compounds $\text{Sc}_5\text{Cl}_8\text{C}$ and $\text{Sc}_5\text{Cl}_8\text{N}$, *Inorg. Chem.* **26**, 469 (1987).
- [34] Yi.-Y. Wang, Q.-H. Yu, P.-J. Guo, K. Liu, and T.-L. Xia, Resistivity plateau and extremely large magnetoresistance in NbAs_2 and TaAs_2 , *Phys. Rev. B* **94**, 041103(R) (2016).
- [35] F. Hulliger, New representatives of the NbAs_2 and ZrAs_2 structures, *Nature (London)* **204**, 775 (1964).
- [36] S. Furuseth and A. Kjekshus, On the arsenides and antimonides of niobium, *Acta Chem. Scand.* **18**, 1180 (1964).
- [37] Y. Li, L. Li, J. Wang, T. Wang, X. Xu, C. Xi, C. Cao, and J. Dai, Resistivity plateau and negative magnetoresistance in the topological semimetal TaSb_2 , *Phys. Rev. B* **94**, 121115(R) (2016).
- [38] P. Jensen, A. Kjekshus, and T. Skansen, The crystal structures of Mo_2As_3 and W_2As_3 , *Acta Chem. Scand.* **20**, 1003 (1966).
- [39] M. Conrad and B. Harbrecht, Synthesis of tantalum tellurides: The crystal structure of Ta_2Te_3 , *J. Alloys Compd.* **187**, 181 (1992).
- [40] A. Hayashi, Y. Ueda, K. Kosuge, H. Murata, H. Asano, N. Watanabe, and F. Izumi, Cation distribution in $(\text{M}', \text{M})_3\text{Se}_4$: I. $(\text{Cr}, \text{Ti})_3\text{Se}_4$, *J. Solid State Chem.* **67**, 346 (1987).
- [41] V. I. Larchev and S. V. Popova, The new chimney-ladder phases Co_2Si_3 and Re_4Ge_7 formed by treatment at high temperatures and pressures, *J. Less-Common Met.* **84**, 87 (1982).
- [42] M. M. Stasova, Crystal structure of bismuth selenides and bismuth and antimony tellurides, *J. Struct. Chem.* **8**, 584 (1967).
- [43] J. Evers, G. Oehlinger, and A. Weiss, Crystal structure of barium disilicide at high pressures, *Angew. Chem., Int. Ed. Engl.* **16**, 659 (1977).
- [44] K. Yamana, K. Kihara, and T. Matsumoto, Bismuth tellurides: BiTe and Bi_4Te_3 , *Acta Cryst. B* **35**, 147 (1979).
- [45] Ye. N. Zav'yalov and V. D. Begizov, Sulphotsumoite, $\text{Bi}_3\text{Te}_2\text{S}$ —a new bismuth mineral, *Int. Geol. Rev.* **25**, 854 (1983).
- [46] I. I. Petrov and R. M. Imamov, Electron diffraction study of $\text{PbTe-Bi}_2\text{Te}_3$ phases, *Kristallografiya* **14**, 699 (1969).
- [47] H. J. Mattausch, A. Simon, N. Holzer, and R. Eger, Monohalogenide der Lanthanoide, *Z. Anorg. Allg. Chem.* **466**, 7 (1980).
- [48] R. L. Daake and J. D. Corbett, Zirconium monobromide, a second double metal sheet structure. Some physical and chemical properties of the metallic zirconium monochloride and monobromide, *Inorg. Chem.* **16**, 2029 (1977).
- [49] K. Sakamaki, H. Wada, H. Nozaki, Y. Ōnuki, and M. Kawai, Topochemical formation of van der Waals type niobium carbosulfide $1\text{T-Nb}_2\text{S}_2\text{C}$, *J. Alloys Compd.* **339**, 283 (2002).
- [50] E. Tang and L. Fu, Strain-induced partially flat band, helical snake states and interface superconductivity in topological crystalline insulators, *Nat. Phys.* **10**, 964 (2014).
- [51] Y. Okada, M. Serbyn, H. Lin, D. Walkup, W. Zhou, C. Dhital, M. Neupane, S. Xu, Y. J. Wang, R. Sankar, F. Chou, A. Bansil, M. Z. Hasan, S. D. Wilson, L. Fu, and V. Madhavan, Observation of Dirac node formation and mass acquisition in a topological crystalline insulator, *Science* **341**, 1496 (2013).
- [52] I. Zeljkovic, Y. Okada, M. Serbyn, R. Sankar, D. Walkup, W. Zhou, J. Liu, G. Chang, Y. J. Wang, M. Z. Hasan, F. Chou, H. Lin, A. Bansil, L. Fu, and V. Madhavan, Dirac mass generation from crystal symmetry breaking on the surfaces of topological crystalline insulators, *Nat. Mater.* **14**, 318 (2015).
- [53] H.-X. Deng, Z.-G. Song, S.-S. Li, S.-H. Wei, and J.-W. Luo, Atomic-ordering-induced quantum phase transition between topological crystalline insulator and Z_2 topological insulator, *Chin. Phys. Lett.* **35**, 057301 (2018).
- [54] See Supplemental Material at <http://link.aps.org/supplemental/10.1103/PhysRevB.103.155113> for details of MCN calculations, all bulk bands, and evolutions of the sum of HWCCs.
- [55] G. Kresse and J. Furthmüller, Efficiency of ab-initio total energy calculations for metals and semiconductors using a plane-wave basis set, *Comput. Mater. Sci.* **6**, 15 (1996).
- [56] G. Kresse and J. Furthmüller, Efficient iterative schemes for *ab initio* total-energy calculations using a plane-wave basis set, *Phys. Rev. B* **54**, 11169 (1996).
- [57] J. P. Perdew, K. Burke, and M. Ernzerhof, Generalized Gradient Approximation Made Simple, *Phys. Rev. Lett.* **77**, 3865 (1996).
- [58] P. E. Blöchl, Projector augmented-wave method, *Phys. Rev. B* **50**, 17953 (1994).
- [59] G. Kresse and D. Joubert, From ultrasoft pseudopotentials to the projector augmented-wave method, *Phys. Rev. B* **59**, 1758 (1999).
- [60] D. Gresch, G. Autès, O. V. Yazyev, M. Troyer, D. Vanderbilt, B. A. Bernevig, and A. A. Soluyanov, Z2Pack: Numerical implementation of hybrid Wannier centers for identifying topological materials, *Phys. Rev. B* **95**, 075146 (2017).
- [61] A. A. Soluyanov and D. Vanderbilt, Computing topological invariants without inversion symmetry, *Phys. Rev. B* **83**, 235401 (2011).
- [62] A. A. Mostofi, J. R. Yates, Y.-S. Lee, I. Souza, D. Vanderbilt, and N. Marzari, Wannier90: A tool for obtaining maximally-localised Wannier functions, *Comput. Phys. Commun.* **178**, 685 (2008).
- [63] Q. S. Wu, S. N. Zhang, H.-F. Song, M. Troyer, and A. A. Soluyanov, WannierTools: An open-source software package for novel topological materials, *Comput. Phys. Commun.* **224**, 405 (2018).
- [64] M. P. L. Sancho, J. M. L. Sancho, J. M. L. Sancho, and J. Rubio, Highly convergent schemes for the calculation of bulk and surface Green functions, *J. Phys. F* **15**, 851 (1985).
- [65] C. J. Bradley and A. P. Cracknell, *The Mathematical Theory of Symmetry in Solids: Representation Theory for Point Groups and Space Groups* (Oxford University Press, Oxford, 1972).
- [66] L. Fu and C. L. Kane, Topological insulators with inversion symmetry, *Phys. Rev. B* **76**, 045302 (2007).
- [67] R. D. King-Smith and D. Vanderbilt, Theory of polarization of crystalline solids, *Phys. Rev. B* **47**, 1651 (1993).